AIAA JOURNAL
Vol. 62, No. 6, June 2024

Acoustical Holography and Coherence-Based Noise Source Characterization of an Installed F404 Engine

Logan T. Mathews* and Kent L. Gee†
Brigham Young University, Provo, Utah 84602

https://doi.org/10.2514/1.J063543

Understanding the acoustic source characteristics of supersonic jets is vital to accurate noise field modeling and jet noise reduction strategies. This paper uses advanced, coherence-based partial field decomposition methods to characterize the acoustic sources in an installed, supersonic GE F404 engine. Partial field decomposition is accomplished using an equivalent source reconstruction via acoustical holography. Bandwidth is extended through the application of an array phase-unwrapping and interpolation scheme. The optimized-location virtual reference method is used. Apparent source distributions and source-related partial fields are shown as a function of frequency. Local maxima are observed in holography reconstructions at the nozzle lipline, distinct in frequency and space. The lowest-frequency local maximum may relate to noise generated by large-scale turbulence structures in the convectively subsonic region of the flow. Other local maxima are correlated primarily with Mach wave radiation originating from throughout the shear layer and into the fully mixed region downstream of the potential core tip. Source-elucidating decompositions show that the order and behavior of the decomposition lend to the local maxima being related to distinct subsources. Between the local maxima, however, there may be a combination of sources active, which is likely the cause of the spatiospectral lobes observed in other full-scale, supersonic jets.

Nomenclature

D_j	=	fully expanded jet nozzle exit diameter
$\boldsymbol{H}_{\mathrm{YP}}$	=	transfer matrix
h	=	height of jet centerline
K	=	number of selected virtual references
$\boldsymbol{L}$	=	lower-triangular matrix from Cholesky decomposition
L_c	=	potential core length
$\tilde{L}_c$	=	estimated potential core length
L_s	=	supersonic core length
$\tilde{L}_s$	=	estimated supersonic core length
M	=	number of partial fields in sum
M_j	=	fully expanded Mach number
N	=	number of candidate virtual reference locations
$\boldsymbol{P}$	=	matrix of complex pressures
P_{MUSIC}	=	multiple signal classification power
$\boldsymbol{R}_{\mathrm{noise}}$	=	noise subspace matrix
$\boldsymbol{S}_{xx}$	=	cross-spectral matrix
$\boldsymbol{u}$	=	trial vector
$\boldsymbol{w}$	=	singular vector
$\boldsymbol{W}$	=	matrix of singular vectors
x	=	distance downstream of jet nozzle axis
$\boldsymbol{X}$	=	virtual-reference-selected complex pressures
y	=	horizontal distance from jet centerline
$\boldsymbol{Y}$	=	near-field acoustical holography-reconstructed complex pressures
z	=	vertical distance from the ground plane
γ_{ij}^2	=	coherence
$\boldsymbol{\Sigma}$	=	diagonal matrix of singular values

Presented as Paper 2023-3212 at the AIAA Aviation 2023 Forum, San Diego, CA, June 12–16, 2023; received 6 September 2023; revision received 27 December 2023; accepted for publication 26 February 2024; published online 23 April 2024.

*Graduate Student, Department of Physics and Astronomy; loganmathews@byu.net. Student Member AIAA.

†Professor of Physics, Department of Physics and Astronomy; kentgee@byu.edu. Associate Fellow AIAA.

I. Introduction

NOISE from high-performance military aircraft remains a significant concern for both communities adjacent to military installations and for those who work near the aircraft. Significant progress in the characterization and understanding of supersonic jet noise has been made; however, there remains much to be discovered about the noise sources. Particularly, the observation of multiple-lobed behavior in these supersonic jets [1–9] and a study of lobe properties suggest the existence of several active, quasi-independent, acoustic sources in the plume [5,8]. While hypotheses have been proposed for this multilobe phenomenon [10,11], none have yet proved conclusive.

Decomposition of acoustic fields can be a powerful tool for characterizing and localizing sources [12–14]. The ability to isolate independent sources into separable fields can provide significant insight into the location, extent, and behavior of such acoustic sources. While a variety of decomposition methods are available, the most useful source-elucidating decompositions separate independent acoustic sources accurately and with physical relevance, providing a basis for the jet noise field in terms of individual source contributions [15]. However, achieving such decomposition is challenging. If a sound field is created by multiple incoherent sources, the separability of the field is ensured, and the result is obtained straightforwardly. However, given the partial coherence of jet noise, the subsources can be considered neither completely coherent nor incoherent. The existence of multiple sources of noise with finite mutual coherence makes performing source decomposition difficult. Many traditional decomposition techniques, such as singular value decomposition (SVD), can produce nonunique results that depend on reference locations, and thus the resulting partial fields (PFs) are not guaranteed to be tied to physical sources [16]. Therefore, the development of methods to elucidate such sources is vital for producing physically meaningful results.

One such method, the optimized-location virtual reference (OLVR) algorithm, was developed by Wall et al. [17] for use in the analysis of supersonic jet noise. This method works in conjunction with near-field acoustical holography (NAH) to provide a physically meaningful PF decomposition (PFD) based on virtual references (VRs) that are placed near the presumed acoustic source using a NAH reconstruction. Candidate VRs are assigned a likelihood of being near an acoustic source, and VRs are selected to be separated by a coherence criterion, thus increasing the probability of targeting

independent (or poorly correlated) sources. The PF decomposition is then performed using these VRs as a guide for separating the field.

To achieve meaningful decompositions, however, a mesh of sufficient resolution must be available to separate acoustic fields near the source. For this task, acoustical holography is used to provide a reconstruction of the acoustic field at the nozzle lipline, where the OLVR decomposition can then be performed. In this paper, statistically optimized near-field acoustical holography (SONAH) is employed. Acoustical holography in some form has been applied to jet noise analyses previously by Wall et al. [3] and Leete et al. [5] for full-scale installed tactical engines, by Lee and Bolton [39], Long [18], Vold et al. [19], and Shah et al. [38] for laboratory-scale jets, and by Leete et al. [58] for a large-eddy-simulated supersonic jet.

Jet mixing noise is produced by the interaction of convected turbulence structures with the surrounding atmosphere. In supersonic, shock-containing jets, turbulence structures can interact with the shock cells to create a secondary source of noise, of which there are two divisions (broadband shock-associated noise and screech). While shock-associated noise is an important noise component of shock-containing jets, this paper focuses on mixing noise in supersonic jets, which is the dominant sound source in most full-scale tactical aircraft [20,21]. Within the realm of mixing noise, it has been suggested that there are two primary scales of turbulence that have differing radiative characteristics [22]. Smaller turbulence structures have been associated with omnidirectional noise radiation, while larger turbulence structures tend to radiate preferentially at angles of 110–160° relative to the jet inlet, depending on their convective speeds. Based on this understanding of jet noise, Tam et al. [23,24] have developed a two-source model for jet noise that uses these two categories to explain the spectral components of jet noise. In this framework, mixing noise is composed of large-scale structure noise (LSN) and fine-scale structure noise (FSN). Tam [25] suggested that LSN is primarily associated with Mach wave radiation (MWR) from supersonically convecting turbulence structures and that it is driven principally by the Kelvin-Helmholtz (K-H) mechanism. However, we note that throughout the literature, MWR and LSN have been used in a variety of contexts, and there are no universally agreed-upon uses of these or like terms. As such, we will adopt a particular definition of these terms for this paper and attempt to describe other findings accordingly.

This two-source model has been used widely in modeling the spectral characteristics of jet noise [19,20,26,27]. However, the two-source model has been found to not fully reproduce the spectral component of measured jet noise, specifically in full-scale tactical engines at high powers, including the T-7A aircraft used in this study [10,20,28]. Recent studies have suggested that noise from large-scale turbulence structures may not be associated with only one mechanism. Liu et al. [11] studied the effect of temperature ratio on radiated noise using large-eddy simulations. They found that with an increasing temperature ratio, directional mixing noise separated into two distinct noise components: one low-frequency component consistently radiating at 150° and one that radiated at higher frequencies and more upstream angles with an increasing temperature ratio. They associated the first component with what they termed LSN and the second with MWR. Likewise, Prasad and Morris [29] noted two noise components associated with large-scale turbulence structures: one related to the K-H instability that exhibited MWR, and another that exists as the flow decelerates beyond the potential core. In terms of wavepackets, Jordan and Colonius [30] described two different noise components associated with large-scale turbulence structures; one supersonic, generating noise through MWR, and another subsonic, which "leaked" noise through spatial modulation ("jitter"). Similarly, Schmidt et al. [14] identified two types of wavepackets present in supersonic jet turbulence. These were associated with the K-H and Orr-type instability waves. Their results suggested that the K-H instability existed primarily upstream of the potential core, while the Orr-type mechanism was active downstream of the potential core. While these studies were done in different paradigms and do not result in a complete, consistent framework for mixing noise radiation from supersonic jets, we simply note that they all suggest that there are at least two distinct noise radiation components. There is one higher-frequency noise component that originates farther upstream, generally radiates at >140°, and is associated with MWR from convectively supersonic turbulence structures. There is a second noise source that is localized further downstream, has a lower characteristic frequency, radiates at 140–160°, and may be associated with radiation from convectively subsonic turbulence. In this paper, we refer to the first component as MWR and the second as LSN.

The purpose of this paper is to investigate source-related characteristics and radiation phenomena of an installed, GE F404 engine using advanced PFD methods. Distinct local maxima are observed in acoustical holography reconstructions near the nozzle lipline. Multilobe radiation behavior in the field is observed at frequencies between local maxima. The OLVR method is used to produce source-elucidating PFs. OLVR decompositions show that, at frequencies where multilobed radiation in the field is observed, PFs containing distinct radiation lobes are present. From this, it is hypothesized that the local maxima likely correspond to distinct subsources involving phenomena such as MWR and LSN, and that multilobed radiation behavior is likely occurring due to the activity of distinct acoustic source regimes within the flow.

II. Methods

A. Measurement

The Boeing/Saab T-7A Red Hawk is an advanced jet trainer aircraft developed for the United States Air Force and is powered by the F404-GE-103 afterburning turbofan engine. This engine is a further development in the F404 family, which has been the subject of numerous acoustic studies [31–33]. Measurements were made in six runs of five different engine conditions: 75% N2, 82% N2, 88% N2, military power, and maximum afterburner (AB). The analyses in this paper will focus on the AB engine condition, with all six runs being concatenated for more averaging. At AB, the fully expanded Mach number (M_j) of the overexpanded jet is estimated to be 1.46, with TTR = 6.9 [34].

Acoustic data were obtained from an extensive measurement of the T-7A aircraft at Holloman Air Force Base in August 2019. Details of the measurement are provided by Leete et al. [6]. Numerous microphone arrays were deployed to measure the aircraft; however, this study focuses on a 120-element ground array placed near the aircraft, shown in Fig. 1a. A schematic of this array is shown in Fig. 1b and is referred to as the imaging array for its primary use in imaging-type

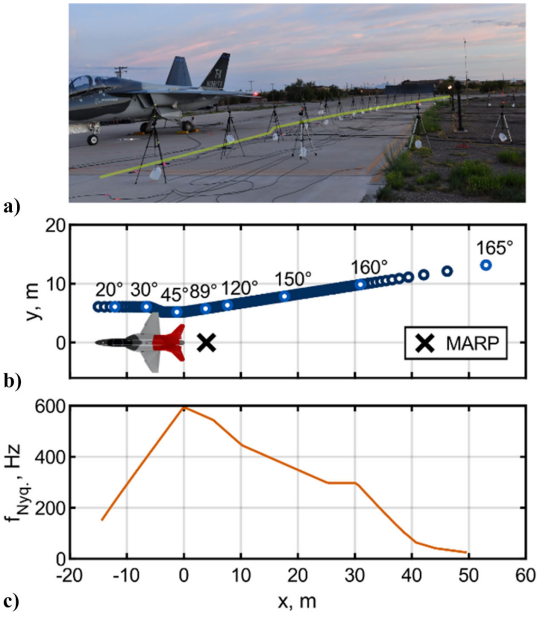

Fig. 1 a) Photograph of T-7A aircraft measurement with ground-based microphone array highlighted in yellow. b) Schematic of the array. c) Spatial Nyquist frequency of the array.

analyses such as acoustical holography and beamforming. The array spans a nearly 70 m aperture, from 15 m in front of the exit plane to ∼55 m downstream of the nozzle exit. To produce such an aperture with 120 microphones, element spacing was varied based on the expected frequency content as determined by studying prior full-scale jet noise studies, including those by Wall et al. [1], Tam and Powers [10], and Leete et al. [5], among others. The spatial Nyquist frequency for each microphone pair in the array is shown in Fig. 1c. The portion of the array near and ahead of the microphone array reference point (MARP; located at $x = 3.96$ m) was configured with relatively close microphone spacing, resulting in a higher spatial Nyquist frequency to accommodate broadband shock-associated noise (BSN) and other noise with significant high-frequency content. Notably, elements far downstream were given much greater spacing because of the anticipated dominance of lower-frequency MWR or LSN. This allowed for a greater aperture to be captured with a limited number of microphones while not sacrificing fidelity in areas where higher-frequency content is expected to dominate.

B. Bandwidth Extension

Conventional acoustic imaging techniques are bandwidth-limited by the spatial separation of transducers in the measurement. Such limitations ordinarily constrain results to frequencies below the design frequency/spatial Nyquist frequency of the array. Analyses at higher frequencies result in spatial aliasing that compromises the accuracy of the reconstructions. Given the limited number of transducers and large spatial aperture of this measurement, acoustical holography is limited to ∼400 Hz and below at the densest portion of the array. However, significant information about the jet noise source is contained above this frequency (such as the dominant energy from BSN). Thus, pursuing methods for bandwidth extension is needed to provide more information about the broadband jet noise source.

One method of extending the bandwidth of array-based measurements is the unwrapped phase array interpolation (UPAINT) method. This method, adapted from Goates et al. [35], spatially interpolates the magnitude and phase of the cross-spectral matrices (CSMs) produced by the measurement. It has been previously applied to jet noise for beamforming analyses by Harker et al. [36]. The key to this technique is unwrapping the aliased phase between each microphone pair in the CSMs. Conventional unwrapping techniques may be used; however, this paper applies a coherence-based pairwise phase unwrapping technique discussed by Cook et al. [37] that is well suited to partially coherent broadband signals such as those associated with jet noise. With the application of these methods, the results shown in this paper extend far above the array design frequency, presently validated up to a frequency of 1 kHz ($\sim Sr \leq 0.5$). A brief overview of the UPAINT procedure implemented for this study is given here for reference.

Phase unwrapping is accomplished in a microphone pair-by-pair sense across frequency. It should be noted that phase unwrapping spatially across the array, one frequency at a time (i.e., a 2D phase unwrapping of the CSM at a given frequency), can lead to significant errors. Spatial phase unwrapping, while producing visually acceptable results at each frequency, guarantees no meaningful phase relationship across frequencies. Thus, phase unwrapping must be undertaken across the frequency dimension for each microphone pair.

A CSM $\boldsymbol{C}$ may be defined from the computed complex pressures along the array as

$$\boldsymbol{C}(f) = \frac{1}{m}\boldsymbol{p_h}\boldsymbol{p_h}^H = \begin{bmatrix} G_{11}(f) & \cdots & G_{1m}(f) \\ \vdots & \ddots & \vdots \\ G_{m1}(f) & \cdots & G_{mm}(f) \end{bmatrix}$$

where $\boldsymbol{p_h} = \boldsymbol{p_h}(f)$ is the computed complex pressures along the array, m is the number of measurement points in the array, and $G_{ij}(f)$ is the cross-spectrum between the ith and the jth array elements.

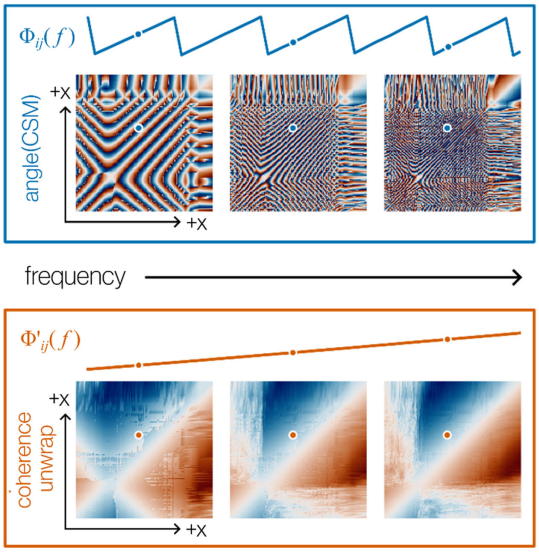

Fig. 2 Illustration of phase unwrapping on cross-spectral matrices. The unwrapped phase is shown above, and the coherence-unwrapped case is shown below.

The magnitude $|\boldsymbol{C}(f)|$ and phase $\boldsymbol{\Phi}(f) = \arg\{\boldsymbol{C}(f)\}$ may be computed directly from the CSM. Phase unwrapping is then accomplished for each given $\Phi_{ij}(f) \in \boldsymbol{\Phi}(f)$. While the methodology for standard phase unwrapping is discussed in Goates et al. [35], a coherence-based phase unwrapping technique for $\Phi_{ij}(f)$ is discussed here.

Signal coherence becomes an important factor in phase unwrapping when there is poor coherence between the two signals considered. Therefore, coherence is used as a criterion in the unwrapping process to reduce nonphysical phase unwrapping. First, for a given $\Phi_{ij}(f)$, points are classified based on whether they have sufficient coherence to allow for accurate phase unwrapping. This is done by selecting some coherence threshold value or scheme to classify points based on their relative coherence. Further discussion on the particular method used here is given by Cook et al. [37]. Then, a two-part scheme is used to unwrap the signal. First, those points above the coherence threshold are conventionally unwrapped. Then, a least-squares method is used to unwrap the remaining subthreshold points based on a selection of the closest neighboring unwrapped super-threshold points. This provides phase unwrapping for the entire signal while reducing the errors introduced by low coherence. An illustrative example of such an unwrapping scheme is shown in Fig. 2, where CSM phases are shown for three distinct frequencies. Axes have been added to show the spatial order of the CSM points in terms of x position. The direction of increasing frequency is indicated by an arrow. The phase relationship as a function of frequency for a given pair of microphones ($\Phi_{ij}(f)$) is shown above, where the microphone pair is indicated by the markers on the CSMs. The results of coherence-unwrapping each pair, $\Phi'_{ij}(f)$, is shown below. In this case, the signals are quite coherent, leading to a linear phase relationship.

C. Acoustical Holography

SONAH is an inverse method developed for a variety of acoustic problems and has been applied to jet noise sources [3,38–40]. An overview of the SONAH process is given here, but more detailed descriptions may be found in Refs. [41,42], with application to jet-noise-specific problems in Refs. [3,5]. The SONAH process is a method of leveraging a limited measurement array (often referred to as the hologram) to reconstruct acoustic properties at locations of interest. The SONAH process also involves certain techniques to address a limited-aperture measurement of a partially coherent jet noise source.

First, synchronously measured time-domain pressure signals across the array are Fourier-transformed to create frequency-dependent CSMs that contain both amplitude and phase information.

Multiple run-ups of the engine are used to increase the number of blocks to average over in determining CSMs. Second, the field is decomposed into partial, self-coherent fields using an SVD method. Third, various enhancements are made to mitigate finite aperture and discrete spatial sampling limitations, such as a numerical aperture extension using an analytic continuation method (see Ref. [43]), interpolation, etc. Then, it is assumed that the acoustical behavior at the hologram can be represented as a linear combination of wavefunctions (in a matrix $\boldsymbol{A}$) that satisfies the linear equation

$$\boldsymbol{Ac} = \boldsymbol{p_h} \tag{1}$$

where $\boldsymbol{c}$ is a vector of unknown coefficients and $\boldsymbol{p_h}$ is a vector of measured complex pressures at the hologram. The SONAH algorithm applied in this paper uses an equivalent wave model (EWM) based on a set of cylindrical wave functions defined relative to an axis along the jet centerline. These basis functions, composed of Hankel functions for the radial component and complex exponentials for the azimuthal and x dependence, are given by

$$\Psi_{l,k_x}(r,\phi,x) \equiv \frac{H_l^{(1)}(k_r r)}{H_l^{(1)}(k_r r_0)} e^{il\phi} e^{ik_x x},\ r \geq r_0 \tag{2}$$

where r is defined as the radial distance from the jet centerline, r_0 is the radius of the reference surface where r_0 is chosen to be an appreciably small number (in this case $r_0 = 0.5$ mm), and the radial wavenumber k_r is determined by

$$k_r = \begin{cases} \sqrt{k^2 - k_x^2}, & |k| \geq |k_x|, \\ i\sqrt{k_x^2 - k^2}, & |k| < |k_x| \end{cases} \tag{3}$$

where the second case accommodates evanescent radiation, thus accomplishing the near-field portion of SONAH.

In this paper, only the $l = 0$ (axisymmetric) case is considered for the set of wavefunctions. Due to the measurement array being confined to the ground, the representation of higher-order azimuthal modes would be inaccurate. In addition, Leete et al. [44] showed favorable azimuthal coherence up to several hundred hertz for a high-performance military jet, lending credence to the inclusion of only the axisymmetric wavefunctions for this paper. The complete EWM is then formed as the matrix $\boldsymbol{A}$, given as

$$\boldsymbol{A} = \begin{bmatrix} \Psi_1(r_{h1}) & \cdots & \Psi_1(r_{hm}) \\ \vdots & \ddots & \vdots \\ \Psi_N(r_{h1}) & \cdots & \Psi_N(r_{hm}) \end{bmatrix} \tag{4}$$

where N is the number of wavefunctions used, r_{hv} is the radial distance of the vth measurement (hologram) point, and m is the number of measurement (hologram) points. A sufficient number of wavefunctions are generated to construct an effectively complete basis over a source-free region of interest. While no analytical criterion exists for determining what constitutes a complete basis in SONAH, a complete basis is effectively achieved when the addition of additional wavefunctions produces no change in the solution. Additional discussion on the selection of wavefunctions in $\boldsymbol{A}$ is given by Hald [42]. In essence, the matrix $\boldsymbol{A}$ is a transfer matrix from the hologram to a reference surface very close to the jet centerline. The inverse problem is then formulated as

$$\boldsymbol{c} = \boldsymbol{A}^{-1}\boldsymbol{p_h} \tag{5}$$

In practice, $\boldsymbol{A}$ is nonsquare, and the inversion is nontrivial. Depending on the dimensions of $\boldsymbol{A}$, the solution is obtained in either a least-squares or minimum-norm sense via a regularized inverse. This process results in the statistically optimized portion of SONAH, as the optimal solution is determined in solving the system [45]. Since holography involves an inward propagation of the field, noise present in the signals can quickly blow up, resulting in large errors in the reconstruction. To filter out high-order wavenumbers associated with nonacoustic noise, a modified Tikhonov regularization method [46] is employed, which acts as a low-pass filter. Once the inverse problem has been solved, a matrix $\boldsymbol{\alpha}$ is created to propagate out to reconstruction locations:

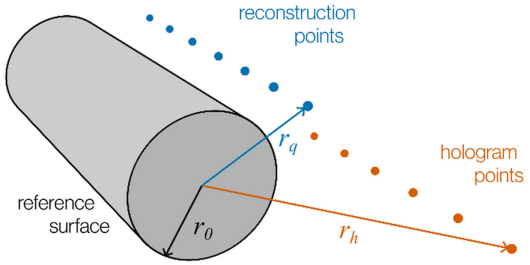

Fig. 3 A diagram showing the holography geometry with hologram (measurement) points, reconstruction points, and the reference surface.

$$\boldsymbol{\alpha} = \begin{bmatrix} \Psi_1(r_{q1}) & \cdots & \Psi_1(r_{qn}) \\ \vdots & \ddots & \vdots \\ \Psi_N(r_{q1}) & \cdots & \Psi_N(r_{qn}) \end{bmatrix} \tag{6}$$

where n is the number of reconstruction locations and r_{qw} is the radial distance of the wth reconstruction point. Figure 3 provides an illustration of the geometry for this holography process, with the reference surface of radius r_0, hologram points at radius r_h, and the reconstruction points at radius r_q.

Like the matrix $\boldsymbol{A}$, $\boldsymbol{\alpha}$ serves as a transfer matrix from the reference surface out to various reconstruction locations. The inverse problem can then be leveraged to predict acoustic properties at the reconstruction locations by evaluating the linear equation

$$\boldsymbol{p_q^T} = \boldsymbol{c\alpha} = \boldsymbol{p_h^T R_{A^H A} A^H \alpha} \tag{7}$$

where $\boldsymbol{R_{A^H A}}$ is the regularized pseudoinverse of $\boldsymbol{A^H A}$. Thus, the acoustic behavior at reconstruction locations is obtained from the hologram via a two-step transfer process. The SONAH process shown here is applied to complex acoustic pressure; however, its application can be extended to particle velocity as well, enabling the construction of acoustic intensity [47]. This paper focuses only on the acoustic pressure results.

D. OLVR Partial Field Decomposition

The OLVR methodology has been previously applied to jet noise measurements by Wall et al. [17]. This technique, however, is largely adapted from a PFD technique described by Kim et al. [16], who essentially showed that using VRs selected using a source-elucidating procedure to decompose the field produces physically meaningful PFs, closely mimicking the expected PFs in a laboratory experiment.

1. *NAH Reconstruction*

To elucidate information about the jet noise source, references should be placed near the jet such that source-related phenomena can be resolved. Kim et al. [16] found that the best PFD results were obtained when references were placed as close as possible to the physical sources. However, placing acoustic sensors near the jet is problematic, and thus an acoustic imaging method is employed to project measurements from a more distant location to near the jet, where VRs can be placed. In this application, SONAH is used to reconstruct the acoustic field at the nozzle lipline, a reasonable proxy for the acoustic source of a jet.

SONAH is an SVD-based NAH method that is used to provide accurate reconstructions of sound fields with multiple sources of limited mutual coherence. The SONAH formulation expresses

measured acoustic properties at a microphone array (called the hologram, see Fig. 4a) as a linear combination of appropriately chosen wavefunctions that form a basis for the acoustic field. This poses an inverse problem, where the wavefunction coefficients are determined in a least-squares or minimum-norm sense, producing the best fit of the chosen basis to the measured acoustic field. This set of wavefunctions and optimized coefficients comprises the EWM, which can be evaluated at other points of interest and can be thought of as a transfer operator that projects the measurement onto a desired surface or field of interest. This can be summarized as

$$\boldsymbol{Y}' = \boldsymbol{H}_{\mathrm{YP}}\boldsymbol{P}$$

where $\boldsymbol{P}$ is the measured hologram, $\boldsymbol{Y}'$ are the reconstructed complex acoustic pressures, and $\boldsymbol{H}_{\mathrm{YP}}$ is the transfer matrix determined by the SONAH algorithm.

To address multiple sources with limited mutual coherence, SONAH relies on an SVD-based PFD to separate the measured signals into energetically ordered, self-coherent PFs. This is done before the EWM is determined; thus, the EWM is computed for each PF, and the resulting field reconstruction is represented as an energetic sum of the resulting PFs.

2. *Selection of Virtual References*

With an equivalent source representation produced through NAH, VRs can then be placed in the field, which will provide a new basis for separation into physically meaningful PFs. Notably, VRs can be placed anywhere in the field with NAH. In this paper, candidate VRs are placed along the jet lipline (represented in Fig. 4a) to attempt the separation of independent source mechanisms. Candidate VR locations were further spatially restricted to be no farther downstream than the point where the level at the lipline was less than 20 dB from the maximum value. This restriction ensures that candidate locations are placed in regions where meaningful energy is being emitted. The OLVR algorithm uses two subroutines to select VRs: a metric for determining the likelihood of sources in the vicinity of a VR and a spatial coherence-based separation of VRs.

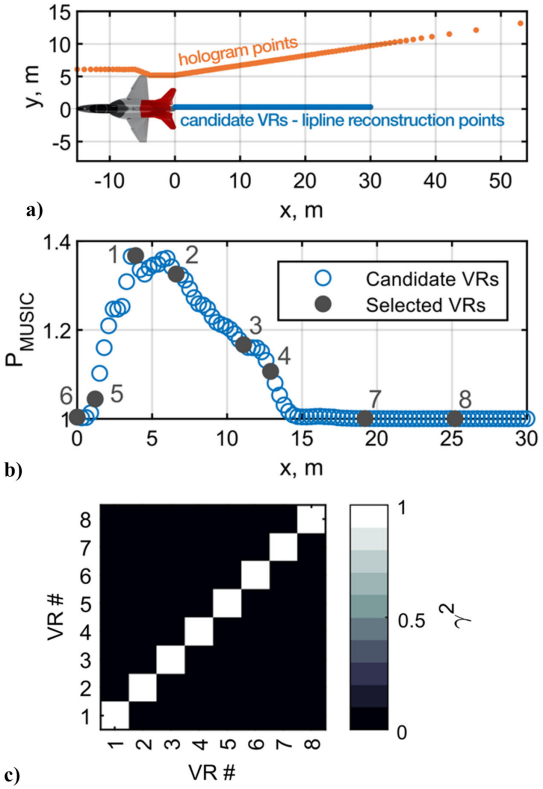

Fig. 4 Outline of VR selection scheme. a) Measured hologram and candidate VRs. b) MUSIC power at candidate and selected VRs. c) Coherence between selected VRs.

To select VRs that are likely to be near acoustic sources, the multiple signal classification (MUSIC) power [48–50] is computed at each candidate VR location. The MUSIC power algorithm provides an estimate of the likelihood that an acoustic source is located at any given point. To calculate the MUSIC power, the CSM at each candidate VR location, $\boldsymbol{S}_{yy}^{N\times N}$, is estimated for every SVD PF; that is,

$$\boldsymbol{S}_{yy}^{N\times N} = \boldsymbol{Y}\boldsymbol{Y}^{H}$$

where $\boldsymbol{Y}^{N\times L}$ is a vector of reconstructed complex pressures at each candidate VR location. Following this, the CSMs are decomposed via SVD to obtain

$$\boldsymbol{S}_{yy}^{N\times N} = \boldsymbol{W}\boldsymbol{\Sigma}\boldsymbol{W}^{H}$$

where $\mathrm{diag}(\boldsymbol{\Sigma}^{N\times N})$ are the singular values and the unitary matrix $\boldsymbol{W}^{N\times N} = [\,\boldsymbol{w}_1\ \boldsymbol{w}_2\ \cdots\ \boldsymbol{w}_N\,]$ contains the associated singular vectors. If there are $K \leq N$ independent sources in the field, then there are K source-related and $N-K$ noise-related singular vectors. Thus, the signal space can be partitioned into two subspaces—one associated with noise and one associated with sources. The noise subspace, $\boldsymbol{R}_{\mathrm{noise}}^{N\times N}$, is calculated as

$$\boldsymbol{R}_{\mathrm{noise}}^{N\times N} = \sum_{n=K+1}^{N} \boldsymbol{w}_n \boldsymbol{w}_n^{H}$$

In practice, determining the order of K for a jet noise source is a heuristic. The jet noise source, composed of turbulence, has no finite number of sources but a quasi-ergodic distribution of turbulent perturbations. Thus, K must be chosen to represent the total field appropriately. Similar to the approach used by Wall et al. [17], K was chosen to be the number of singular values in $\boldsymbol{\Sigma}$ within 20 dB of $\max(\boldsymbol{\Sigma})$. This criterion was chosen to be less than the 40 dB in Ref. [17], as the number (and spatial extent) of VRs in this paper are fewer. While this method produces favorable results, further investigation into the estimation of K is warranted.

The noise subspace is then used to determine the MUSIC power at each candidate location. Given the orthogonality of the SVD, $\boldsymbol{R}_{\mathrm{noise}}$ is orthogonal to the span of the source-related singular vectors. This is exploited in the determination of the MUSIC power. To calculate the MUSIC power, a trial vector is used to "sift" the noise subspace for likely sources. The trial vector is defined as

$$\boldsymbol{u}_n^{N\times 1} = [0\ \cdots\ 0\,1\,0\ \cdots\ 0]^{T}$$

where the vector is composed of zeros, with only the nth component being unity. The trial vector is, however, alterable based on the type of source, with further discussion given by Kim et al. [16]. This version of the trial vector assumes point (monopole) sources; however, a trial vector could be designed that assumes a particular source distribution. Further investigation into trial vectors for jet noise sources is needed. The MUSIC power is then calculated for the nth candidate location as

$$P_{\mathrm{MUSIC}} = \frac{1}{\boldsymbol{u}^{T}\boldsymbol{R}_{\mathbf{noise}}\boldsymbol{u}}$$

This routine is performed for each of the N candidate VR locations. Due to the orthogonality of the source- and noise-related subspaces, if $\boldsymbol{u}_n^{N\times 1} = \boldsymbol{w}_n^{N\times 1}$ for $n = 1$ to K (the source-associated singular vectors), the denominator approaches zero and the MUSIC power becomes infinite. Thus, if the assumed source distribution, $\boldsymbol{u}_n^{N\times 1}$, matches the "actual" source distribution, the MUSIC power becomes large. Thus, higher values of the MUSIC power calculated with the trial vectors indicate a higher likelihood of being near an acoustic source. In practice, with distributed sources and many candidate VR locations, the range of MUSIC powers calculated is relatively small. The finer the resolution of the VR grid (i.e., the larger the value of N), the smaller the variation in the MUSIC power.

If the field contained ideal point sources, the MUSIC power, computed using this trial vector, would theoretically produce a "comb"-like result that would localize the sources precisely. However, with a distributed source, the MUSIC powers form a smoothly varying distribution, as seen in Fig. 4b. If only high MUSIC powers were chosen without considering the location of these points, the separation of sources would be poor. This is because there are redundant VRs that identify the same source. Kim et al. [16] suggest that in the case where the number of incoherent sources is greater than N (i.e., redundancy of candidate VRs is likely), that coherence be used to separate VRs. VRs with high MUSIC power and high mutual coherence likely identify the same source, and thus a set of VRs with high MUSIC power and low mutual coherence is sought.

The search for this set of VRs begins by reordering the complex acoustic pressures of all candidate VRs ($\boldsymbol{Y}^{N\times L}$) in order of MUSIC power as $\boldsymbol{X}'^{N\times L}$, then calculating the associated CSM $\boldsymbol{S}_{yy}^{N\times N} = \boldsymbol{X}'\boldsymbol{X}'^{H}$. From this, the coherence between candidate locations i and j is calculated as

$$\gamma_{ij}^2 = \frac{|S_{ij}|^2}{S_{ii}S_{jj}}$$

where S_{ij} is the ijth component of $\boldsymbol{S}_{yy}^{N\times N}$. Then, an iterative algorithm is used to select the set of VRs with high MUSIC power and low mutual coherence. First, the candidate location with the highest MUSIC power is selected as the first VR. Then, a coherence criterion is chosen (γ_{crit}^2), starting with a low value. The second VR is chosen as the location with the next highest MUSIC power, whose mutual coherence with the previous VR is less than the coherence criterion ($\gamma_{ij}^2 < \gamma_{\text{crit}}^2$). This process is repeated until either K VRs have been identified, or there are no more possible VRs below the coherence threshold. In the latter case, the coherence criterion is then increased, and the process is repeated until a full set of K VRs is found.

Then, a final matrix of coherence-separated, high MUSIC power VRs is constructed as

$$\boldsymbol{X}^{K\times L} = \begin{bmatrix} \boldsymbol{Y}_{R_1} \\ \vdots \\ \boldsymbol{Y}_{R_K} \end{bmatrix}$$

where $\boldsymbol{Y}_{R_k}$ is the R_kth row of $\boldsymbol{Y}^{N\times L}$, with R_k being the index of the kth selected VR.

3. *Decomposition by Virtual References*

The utility of VRs is realized in the decomposition technique. With the selected VRs, $\boldsymbol{X}^{K\times L}$ is decomposed into an orthogonal basis that ideally corresponds to the independent, incoherent sources. The decomposition method used follows the partial coherence decomposition (PCD) method, discussed in detail by Bendat [51]. This method relies upon the Cholesky decomposition to iteratively remove energy from the VR CSM. This CSM is constructed as

$$\boldsymbol{S}_{xx}^{K\times K} = \boldsymbol{X}\boldsymbol{X}^H = \boldsymbol{L}\boldsymbol{L}^H$$

where $\boldsymbol{L}^{K\times K} = [\boldsymbol{l}_1\ \boldsymbol{l}_2\ \cdots\ \boldsymbol{l}_K]$ is a lower-triangular matrix of linearly independent vectors, $\boldsymbol{l}_k$. Due to the nature of the Cholesky decomposition, each vector $\boldsymbol{l}_k$ contains all the energy that is coherent with the kth VR, as the energy is removed iteratively. With this new basis set, the OLVR PFs can then be generated. First, the CSM between all M field points and all K VRs is computed as

$$\boldsymbol{S}_{xy}^{K\times M} = \boldsymbol{X}\boldsymbol{Y}^H$$

Then, the OLVR PFs are generated from this CSM using the basis set as

$$\boldsymbol{P}_{\boldsymbol{x}}^{M\times K} = \boldsymbol{S}_{\boldsymbol{xy}}^{H}(\boldsymbol{L}^H)^{-1}$$

This is the final step in the OLVR algorithm. The resulting OLVR PFs, $\boldsymbol{P}_{\boldsymbol{x}}^{M\times K}$, are separated based on likely, incoherent sources. This increases the likelihood of PFs being physically meaningful since they were generated using VRs of high MUSIC power and low mutual coherence. The OLVR PFs, $\boldsymbol{P}_{\boldsymbol{x}}^{M\times K}$, are necessarily ordered spatially according to the VRs as a byproduct of the decomposition method. For this paper, they are finally re-ordered according to integrated energy from highest to lowest.

III. Results

A. Validation

To provide a first-order validation of the holography method, a reconstruction at the imaging array is compared to the original measurement. Ideally, the reconstructed acoustic behavior should match, but errors are introduced by the holography process. A measured spatiospectral map along the array is presented in Fig. 5 for the AB engine condition. Noticeable in this map is the dominant radiation region, which contracts and moves upstream with increasing frequency. Also visible are spatiospectral lobes, which manifest as distinct local maxima in the map. BSN is manifest near the nozzle at higher frequencies (above $Sr = 0.3$), making a "j"-type shape in the map.

Significant energy is present between $Sr = 0.1$ and $Sr = 0.3$, which is consistent with the general understanding of jet noise in the literature. However, much energy is present well below $Sr = 0.1$, with a large local maximum appearing far downstream around $Sr = 0.05$. It should be noted that the results here are for the afterburning condition, where the TTR approaches seven. Other studies, such as that by Liu et al. [11], have shown the emergence of high-amplitude noise below $Sr = 0.1$ in high TTR jets. It should also be noted that noise from rockets (substantially hotter and faster than jets) exhibits characteristic peak frequencies approximately an order of magnitude lower than other supersonic jets [52,53]. This shift in Strouhal number to lower frequencies with increasing TTR and jet velocity is an open matter of research in the literature.

Figure 6 shows the SONAH reconstruction error at the imaging array for the AB engine condition, with (Fig. 6b) and without (Fig. 6a) the application of the UPAINT bandwidth-extension method. Contours are drawn to show the regions corresponding to the −10 and −20 dB re maximum regions, indicating the areas of greatest energetic importance. Although this preliminary application of the UPAINT algorithm introduces errors upstream and

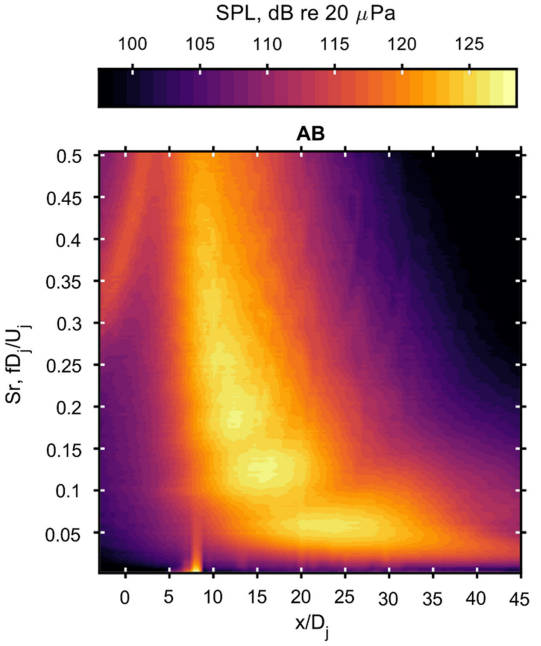

Fig. 5 Measured spatiospectral maps along the imaging array for MIL and AB engine conditions.

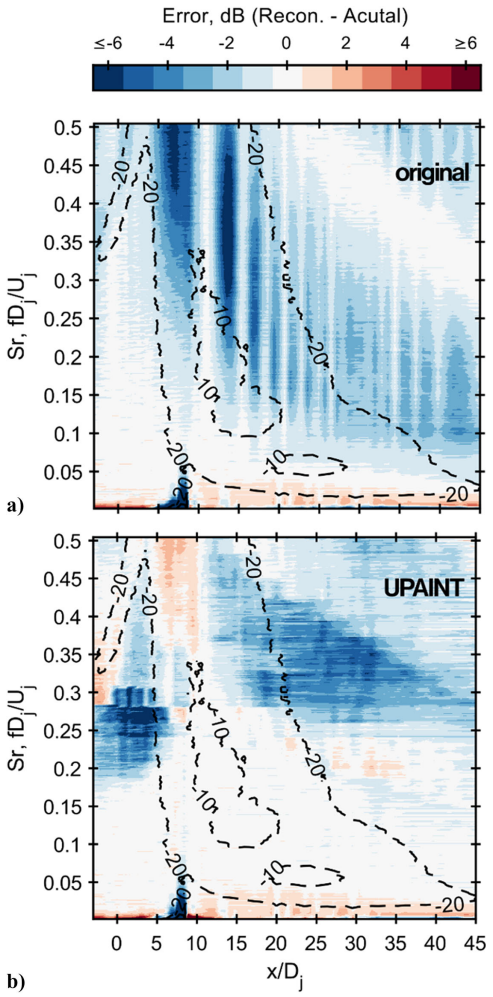

Fig. 6 Reconstruction error at the imaging array for the AB engine condition for a) the original measured data and b) after applying UPAINT.

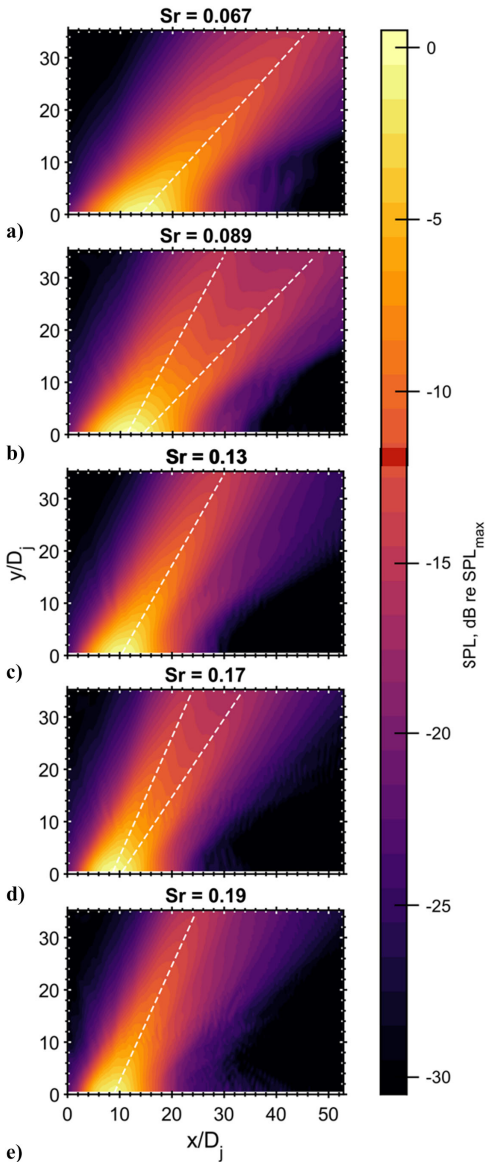

Fig. 7 SONAH reconstruction at AB for five frequencies of interest at the ground plane ($z = 0$).

downstream of the highest amplitude regions (where the signal is relatively low), it is important to note that it significantly improves reconstruction accuracy within the −10 dB contour. While this first application of UPAINT has yielded appreciable improvements in areas of greatest energy, further refinements are being explored to achieve greater accuracy overall, especially in regions with lower amplitude signals. It is worthy of note that, due to the installed nature of this jet, locations near and upstream of the nozzle/aircraft may have aircraft-related scattering. This may account for some of the difficulty in the phase unwrapping and interpolation near the nozzle seen in Fig. 6, since scattering would likely corrupt or mask the true phase information at affected locations, resulting in erroneous phase unwrapping and/or poor interpolation.

B. Field Reconstructions

SONAH field reconstructions at the ground ($z = 0$) are shown in Fig. 7 for the AB condition at five frequencies of interest, which will be discussed further in subsection C. Figures 7a, 7c, and 7e show a single dominant radiation lobe in the field, whose direction has been highlighted by the white dashed lines. However, Figs. 7b and 7d, located at intermediate frequencies, display multilobed radiation behavior, which is also highlighted. Also visible is the trend for the dominant radiation angle to shift forward with increasing frequency. These patterns of single-lobed radiation behavior shifting to multilobed behavior and then back to single-lobed behavior have been observed and characterized with several other installed tactical engines [5,8,70]. These multiple radiation lobes have been commonly referred to as "spatiospectral lobes" due to their manifestation in both space and frequency, and recent investigations have also characterized the temporal structure of these lobes [53].

C. Apparent Source Reconstructions and Local Maxima

A spatiospectral reconstruction is performed at the nozzle lipline as an analogous source representation. As the locations of actual acoustic sources (turbulent structures undergoing rapid convection) are ill-defined, the nozzle lipline serves as a surrogate for the source region. Although the approximate shear layer could be assumed, for the region considered in this analysis, the difference between the two is very small, and the results would be largely equivalent. The reconstruction at the afterburner across a wide range of frequencies along the nozzle lipline is shown in Fig. 8a. Local maxima (LMs) are observed, distinct in frequency and space, and are highlighted by contours corresponding to −1 dB re max level in the enclosed region. These LMs are similar in appearance to those shown for other tactical aircraft by Leete et al. [5] and Wall et al. [3], and they have been postulated to be related to the phenomenon of so-called spatiospectral lobes. The local maxima centers are quasi-harmonic, an observation that has been shared with the spatiospectral lobe phenomenon [54,55]. Several theories have been proposed to explain this nearly harmonic nature of the spatiospectral lobes, including shock–cell interaction [3,5]. However, no definitive explanation has been found

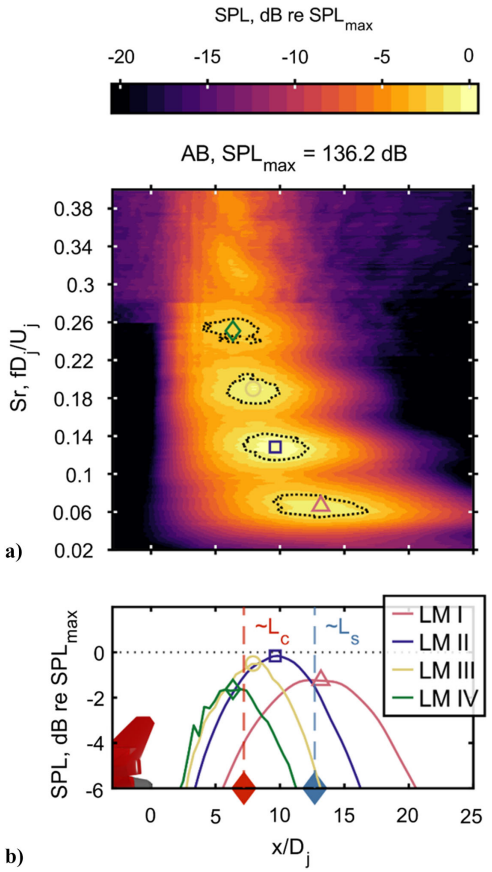

Fig. 8 Apparent source spatiospectral reconstructions at the nozzle lipline at AB. Relative SPL contours are shown for each of the identified local maxima.

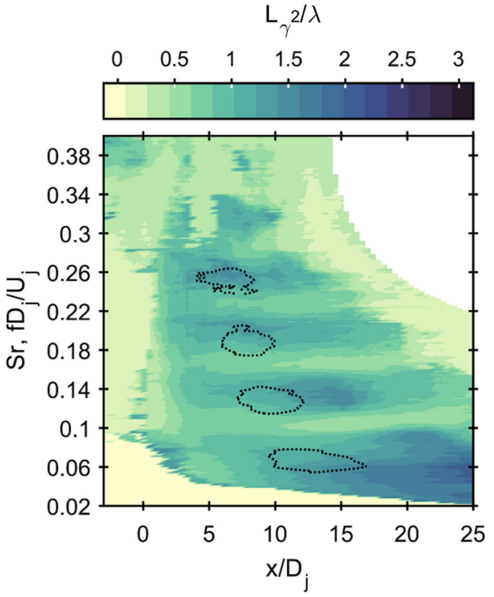

Fig. 9 Acoustic wavelength-normalized coherence length along the nozzle lipline at AB from NAH. LM contours from Fig. 8 are overlain in black dots.

to date. In this reconstruction, four LMs have been highlighted by contours; however, five or more are visible, though their appearances become more irregular at higher frequencies where the performance of the SONAH method begins to degrade. For this analysis, only the first three LMs are considered since they lie within frequencies where the SONAH method is most accurate.

Below the reconstruction (Fig. 8b) are the relative spatial SPL distributions of the first four highlighted LMs. These distributions correspond to the center frequency of each LM. Overlain on the subplots are the approximate locations of the potential and supersonic core tips ($\tilde{L}_c$ and $\tilde{L}_s$, respectively). More discussion on the approximate location of these regions is given in Mathews et al. [56,57]; see also Leete et al. [58] and Liu et al. [11,59,60].

The energetic order of the LMs, from greatest to least, is II, III, I, and IV. Spatially, LM II falls midway between $\tilde{L}_c$ and $\tilde{L}_s$, which has long been regarded as the region of maximum sound power production of the jet [61–63]. While LM II has the greatest amplitude, LM III is only slightly lower in amplitude. Thus, while LM II is well within the region between $\tilde{L}_c$ and $\tilde{L}_s$, the combination of LM II and III peaks very near but just downstream of $\tilde{L}_c$. This is consistent with findings from laboratory-scale heated jets by Baars et al. [64], who observed that the primary flow instability in the jet grew throughout the shear layer, reached a maximum just downstream of L_c, then decayed.

To further characterize the local maxima and their properties, Fig. 9 shows the upstream coherence length normalized by the acoustic wavelength calculated along the nozzle lipline at AB. Although the dimensional coherence length decreases at higher frequencies, caused by a decrease in the characteristic scale of the turbulence producing the noise, this normalization reveals greater self-similarity and allows for a relative comparison of coherence lengths across frequencies [55]. Coherence information was obtained through the SONAH reconstruction. Here, coherence length is defined as the distance required for the coherence between two points to drop from unity to below a threshold of 0.5. The portion of the plot in the upper right corner has been excluded as the reconstruction accuracy in this area is poor, and hence the results in this region are likely nonphysical. It should be noted that this downstream region at high frequencies has low amplitude and contributes very little to the total radiation, and hence any coherence information in this area would be of little value. Overlain on the plot are the contours corresponding to the local maxima from Fig. 8. The areas around the local maxima have a greater normalized coherence length, while the normalized coherence length appears to drop at frequencies between the local maxima. This reinforces the idea that the local maxima represent distinct, quasi-independent radiators. The shortening of the coherence length at frequencies between the LMs where multilobed radiation behavior is present in the field suggests that there may be more uncorrelated sources active. These observations are consistent with the coherence findings of Harker et al. [65] and Swift et al. [55], who showed that local maxima in their data, attributed to the spatiospectral lobe phenomenon, had higher relative coherence.

D. Source Decompositions

Since the LMs indicated in the previous discussion demarcate the most acoustically active frequencies near the source, decompositions can be performed at these frequencies to describe the spatial distribution of potential acoustic sources that contribute to each of these LMs. Additionally, frequencies between these LMs are where multiple-lobed behavior is observed in the field (as seen in Fig. 7), so decompositions can be performed here to identify potentially separate source phenomena present that may contribute to the multi-lobed radiation effect. The OLVR method was used to perform these decompositions. The coherence criteria used and the number of resulting PFs are summarized in Table 1. Note that with increasing frequency, more OLVR PFs (K) were selected in the algorithm, indicating the greater complexity of the field. This has been noticed

Table 1 OLVR process parameters for each frequency analyzed at the AB engine condition

LM#	Sr	γ^2_{crit}	K	M
I	0.067	0.33	4	3
I–II	0.089	0.30	6	4
II	0.13	0.31	7	4
II–III	0.17	0.36	13	7
III	0.19	0.32	9	4

in the field by Swift et al. [55], who showed reduced coherence length with increasing frequency when normalizing by acoustic wavelength. As Wall et al. [66] have shown coherence length to be an important figure of merit in sensing subsources, the result of achieving appreciably low coherence criteria in the decomposition is that the VRs separated are separated by greater than one coherence length. Noticeably, at frequencies between the LMs, more OLVR PFs (K) were required to represent the source, indicating that there are likely more sources of low mutual coherence at these frequencies. For example, LM II requires $K = 7$ PFs, and LM III requires $K = 9$. However, between these LMs, the number of PFs jumps to $K = 13$. Additionally, the number of OLVR PFs at the lipline within 10 dB of the maximum lipline SPL (M) also increased. For example, $M = 4$ for PF II and III, while between them, this jumps to seven. If the LMs do correspond to distinct, incoherent sources, then it would make sense that at frequencies between LMs, where principally two LMs may be contributing to radiation, there would be a greater number of deduced sources of low coherence. In terms of implications for reduced-order models of jet noise, this shows that frequencies around the LMs represent relative local minima in terms of the order of models required, while between the LMs, higher-order models are required to accurately represent full-scale radiation.

Figure 10 shows the results of OLVR decomposition at AB for the five frequencies of interest. Normalized levels of the first 4 OLVR PFs along the nozzle lipline are shown. The resulting energetic sum of the first four OLVR PFs is also shown. At the first frequency (Fig. 10a), the first four PFs produce an accurate representation of the total lipline SPL. As the frequency increases, four PFs become insufficient to accurately reproduce the total energy. This noticeably affects the upstream and downstream areas the most. This is due to a shortening of the coherence length both upstream and downstream at the source as frequency increases, which is shown in Fig. 9. Due to this, more PFs are necessary at these higher frequencies to accurately represent the source.

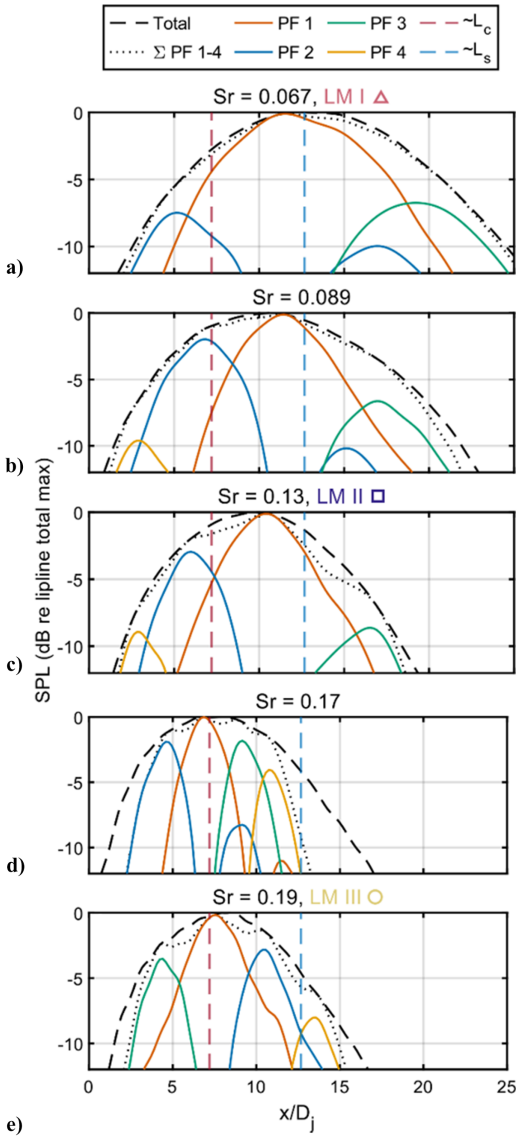

Fig. 10 OLVR decompositions for five frequencies of interest. Relative partial field levels along the lipline are shown.

In examining the OLVR decompositions further, Fig. 10a, corresponding to LM I ($Sr = 0.067$), consists of one primary OLVR PF, with the other remaining PFs being ~6 dB less in peak amplitude. Spatially, this corresponds with the field likely being composed of one principal acoustic source, which appears to be located near $\tilde{L}_s$ as the flowfield transitions locally to fully subsonic behavior. For Fig. 10c, corresponding with LM II ($Sr = 0.13$), there are two dominant sources likely, with the lower amplitude one peaking in the potential core region and the dominant one peaking between $\tilde{L}_c$ and $\tilde{L}_s$. Between LM I and LM II in frequency (Fig. 10b), the decomposition yields a primary PF reaching a maximum just before $\tilde{L}_s$, and a second PF, only about 2–3 dB less in maximum amplitude, near the end of $\tilde{L}_c$. At this frequency, multilobed behavior is observed in total field reconstructions; thus, this decomposition suggests that there are two primary active acoustic sources within 3 dB of the maximum magnitude of each other with low mutual coherence (less than or equal to $\gamma^2 = 0.30$). Spatially, these two likely sources appear to have maxima just before end of $\tilde{L}_c$ and just before the end of $\tilde{L}_s$.

For Fig. 10e, corresponding to LM III ($Sr = 0.23$), there are similar arrangements of the OLVR PFs as in Fig. 10c, with the dominant field (PF 1) reaching a maximum near $\tilde{L}_c$, with another high-amplitude contributing PF in the potential core region (PF 2). Here, though, the PF in the potential core region is of much higher amplitude, being only 2–3 dB lower in amplitude than PF 1. Thus, it appears that LM III may be comprised primarily of radiation from the shear layer region, with the primary source locations being near or upstream of $\tilde{L}_c$. Finally, at a frequency between LM II and LM III, Fig. 10d shows the PF 1 maximum being just ahead of the $\tilde{L}_c$, with LM III being 2–3 dB lower in amplitude, and the other two PFs being ~7–8 dB lower in amplitude than PF 1.

The OLVR decomposition yields PFs that can represent the field accurately in a significantly reduced-order sense. Figure 11 shows the relative error between the total reconstructed holography field and the sum of the first M OLVR PFs at the ground plane, where M has been defined as the number of OLVR PFs within 10 dB of the nozzle lipline maximum value. Dashed contours are drawn on the error plots to demarcate the −10 dB re max region of the field reconstruction. The inclusion of the first M OLVR PFs shows highly accurate representations of the acoustic field within the highest amplitude regions with a relatively small number of PFs. Such results show that reduced-order modeling of jet noise can be accomplished with relatively low-order models at these frequencies of interest. In all cases, the greatest error appears in the upstream direction, where the field is known to have low coherence. This has been accommodated previously in reduced-order models by increasing the order (adding more wavepackets) [67] or by including a secondary compact noise source such as a monopole [68].

To visualize the contribution of each OLVR PF to the acoustic radiation pattern, Fig. 12 shows the total field reconstruction and the first four OLVR PFs for each frequency analyzed on the plane $z = 0$ at AB. Dashed contours are overlain for the −10 dB re max total level. At the frequency corresponding to LM I, PF 1 (Fig. 12b) primarily contributes to the radiation lobe observed in the total field, with PF 2 and PF 3 (Figs. 12c and 12d) contributing up and downstream of PF 1 at significantly lower amplitudes (8–10 dB lower). Similar behavior is observed for LM II and LM III, with the relative amplitudes of higher-order PFs growing. At frequencies between the LMs, multilobe radiation behavior is observed in the total field reconstructions (Figs. 12f and 12p). Between LM II and III in particular, PF 1 and 2 primarily contribute to the dominant lobe

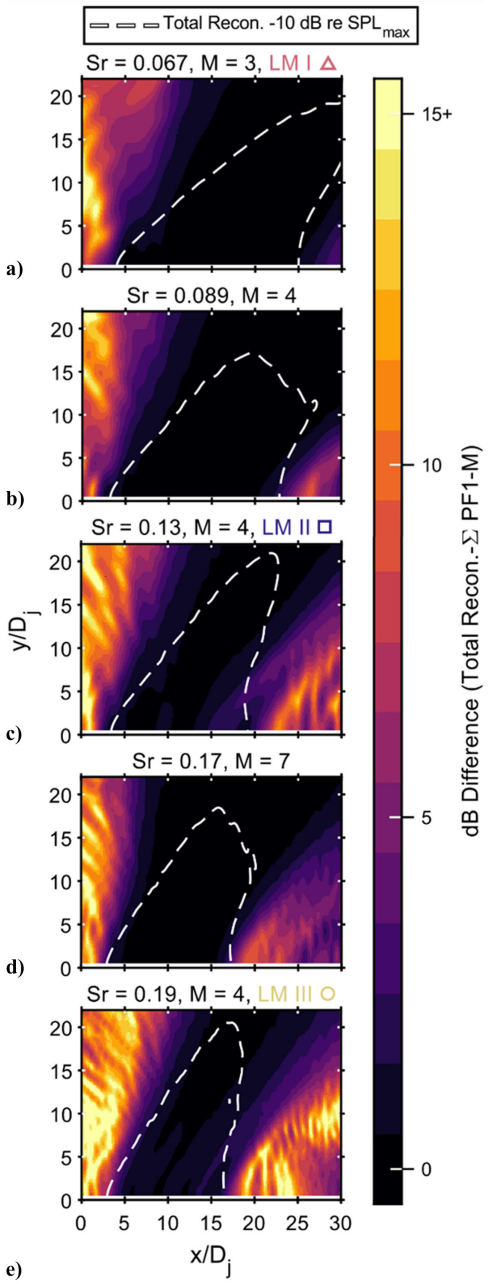

Fig. 11 The relative error at the ground plane is shown between the total reconstruction and the energetic sum of OLVR PFs 1 − *M*.

(Figs. 12q and 12r), while PF 3 contributes mainly to the second, less-energetic lobe (Fig. 12s). Note that at both frequencies between LMs, the OLVR PFs are not strictly contributing to one radiation lobe. This is readily observed in Figs. 12h and 12r. While each of these PFs contributes mainly to one lobe, they retain some energy from the other radiation lobe. This aligns with what is understood about spatiospectral lobes; they have low but finite coherence [55,69,70]; thus, the presence of some energy in each lobe in a given PF is expected. However, there is a possibility of these residues being present in part due to numerical error; however, since a finite coherence criterion was used to select and separate the PFs, this "sharing" of energy is likely due primarily to the coherence between VRs used to decompose the field.

A notable feature of the separated PFs is that at frequencies corresponding to LMs, the PFs have roughly the same directivities, whereas, between the lobes, PFs reflect different directivities. At LM-associated frequencies, the "breaking up" of the single radiation lobe into multiple PFs of similar directivity may be because the source is likely several coherence lengths long. The effect depends on frequency: at $Sr = 0.067$ (LM I), PF1 (Fig. 12b) contains much of the primary radiation. PF 2 and PF 3 (Figs. 12c and 12d) are much lower in amplitude. Thus, the splitting of the most energetic source region has a relatively low effect. At $Sr = 0.19$, however (LM III), PF 1–3 (Figs. 12v–12x) have similar directivities and both have relatively high amplitudes (all within 6 dB of the maximum). This may reflect the most energetic region of the source being more than a coherence length. Harker et al. [65] have shown that coherence length shrinks disproportionately more than the extent of the source region in full-scale supersonic jets; thus, the placement of OLVR VRs greater than a coherence length apart results in splitting the primary source region at higher frequencies into multiple PFs. Thus, even though there are multiple high-amplitude PFs at frequencies corresponding to LMs, they may not be attributable to separate source phenomena, as their directivities (and, by extension, convective velocities) are similar. However, whether or not this is the case remains to be seen.

For the frequency corresponding to LM I, there appears to be one dominant acoustic radiator (shown as PF 1, see Fig. 12b) that contributes primarily to the main radiation lobe. This PF has noticeably more aft-skewed directivity than most of the other frequencies shown. Additionally, PF 1 reaches its maximum level around $\tilde{L}_s$ as seen in Fig. 10a, which is more downstream than the principal PF at any other frequency shown. Given that LSN has been shown to originate farther downstream and have shallower radiation angles [11], it is possible that the dominant noise for LM I may be associated with LSN.

Local maxima II and III have radiation characteristics more in the forward direction, with their most dominant energy coming from upstream of $\tilde{L}_s$. In the case of LM II, the dominant PF has a maximum in between $\tilde{L}_c$ and $\tilde{L}_s$, with the second most energetic PF being just upstream of $\tilde{L}_c$. This could reflect radiation from fully developed turbulence in the region beyond $\tilde{L}_c$ and MWR originating from the shear layer upstream of $\tilde{L}_c$, respectively. LM III, peaking in amplitude around $\tilde{L}_c$, may be primarily associated with MWR originating from the shear layer. Other studies have suggested that MWR from the shear layer and radiation from the fully developed turbulence region beyond $\tilde{L}_c$ exhibit distinct acoustic radiation. Panda et al. [71] observed the correlation between the jet flow and the acoustic field in a laboratory-scale cold jet and found that in convectively subsonic and supersonic jets, correlation with the centerline flow peaked at 10–12 diameters downstream, while correlation with the shear layer peaked at 5–6 diameters downstream, and only for the convectively supersonic case. Viswanathan [72] showed that in convectively supersonic jets, there were two primary sources: one that existed downstream of the potential core and one that was upstream of $\tilde{L}_c$ that was related to strong MWR from the developing shear layer. Thus, we surmise that LM II and III could be related to these two distinct subsources, with the PFs suggesting that both LM II and III could have components from each of these distinct source regions. While this approach has localized potential sources to these regions and has shown that there are likely distinct acoustic sources in these flow regions, connections to distinct radiation mechanisms are strictly corollary; further work with numerical simulations that connect flow and radiated acoustic energy is necessary to prove causality, such as those by Liu et al. [11,31] and Unnikrishnan and Gaitonde [73].

E. Discussion

Connections can be made between phenomena observed here and in other experiments, both lab-scale and numerical. Schmidt et al. [14] showed, in a characterization of jet flow via LES, that structures throughout the shear layer up to L_c were characterized by K-H-type wavepackets, whereas downstream of the potential core and at lower frequencies, modes associated with Orr-type wavepackets were dominant. The Orr mechanism was found to be present in the shear layer upstream of L_c but at a much lower amplitude than the K-H mechanism. This identification of mechanisms seems to be consistent with what has been described

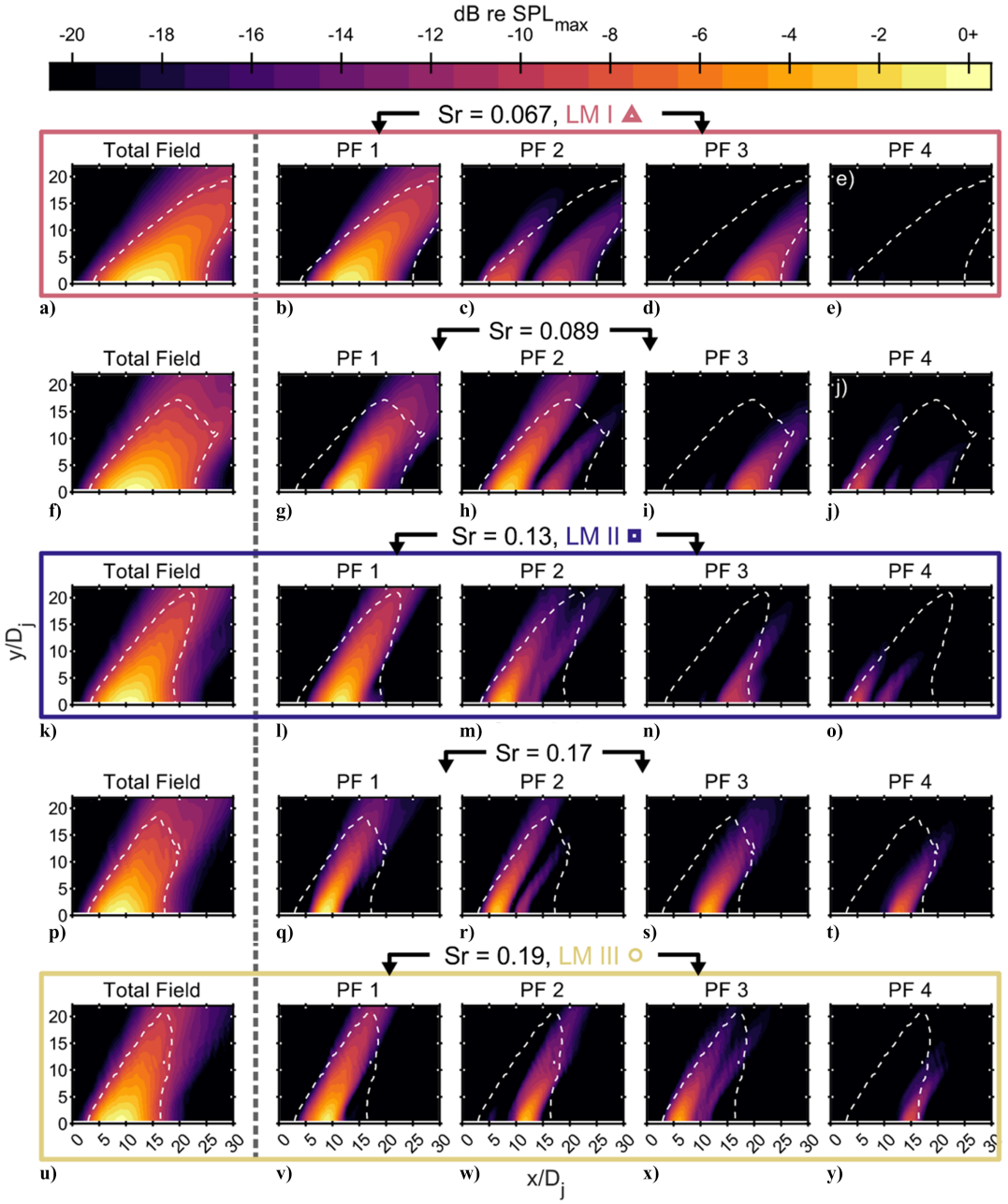

Fig. 12 Total field and first four PFs at AB on the plane $z = 0$. Dashed contours indicate −10 dB re SPL_{max} of the total field. Amplitude scales consistent across each frequency.

elsewhere as the phenomena of MWR and LSN. Liu et al. [11] have shown in acoustic data from LES that MWR appears to originate from throughout the shear layer and continues downstream some distance. This MWR appears to have broadband behavior. LSN was correlated with an acoustically active region located farther downstream with a lower characteristic frequency. This localization of MWR and LSN seems consistent with observed behaviors of the K-H and Orr mechanisms. Additionally, Liu et al. [11] showed that at AB-like conditions, MWR reached a peak intensity at around $Sr = 0.2$, while below $Sr = 0.1$, LSN dominated the radiation. Comparing this with the LM observed in this paper, LM I lies at $Sr = 0.067$ at AB, while LM II and III are in a region that MWR has been suggested to dominate. This reinforces the idea that LM I may principally correspond to LSN (and, by extension, possibly the Orr mechanism), while LM II and III ($Sr = 0.13$ and 0.19) may be primarily attributable to MWR (and therefore, the K-H mechanism in the shear layer and region just after the collapse of the potential core, but before $\tilde{L}_s$). Furthermore, a far-field analysis of the same measurement used in this paper by Christian et al. [34] showed that a convective Mach number associated with the K-H mechanism was most accurate at predicting the peak overall radiation angle of the jet. Thus, given that LM II and III are the two most energetic local maxima, it is indeed likely that they are associated with the K-H mechanism.

IV. Conclusions

A coherence-based acoustic source decomposition has been performed at the maximum afterburner engine condition for an installed GE F404 engine using reconstructions obtained via acoustical holography. The application of a phase-unwrapping and interpolation method increases the bandwidth of acoustical holography applied to jet noise fields.

These analysis tools have been applied to source characterization efforts. Apparent source representations at the nozzle lipline show LMs, distinct in space and frequency, at both engine conditions. These local maxima occur further upstream with increasing frequency.

Decompositions at and between the frequency centers of the first three local maxima show lower overall numbers of PFs required for representing the field at the LM centers, while between the LMs, relatively more PFs are required. Likewise, at frequencies between the LMs, more PFs are higher in amplitude than at the LM centers. This suggests lower coherence between the LM centers, and that the field between LMs is likely a combination of the phenomena constituting each LM. It seems likely that the first LM may be caused primarily by subsonic noise radiation from large-scale turbulence structures, while higher-order LMs may correspond mainly to MWR originating from different regions of the flow—the shear layer and the region just after the collapse of the potential core but before the end of the supersonic core.

While these results are promising, significant research remains. While analyses of full-scale installed engines such as this are useful for identifying real-world acoustic phenomena, additional tools and analyses are required to directly connect and understand the relationship between flow structure and acoustic radiation phenomena. Ultimately, a proper understanding of supersonic jet noise must be fostered by a combination of complementary full-scale analyses, laboratory-scale experiments, and numerical simulations.

Acknowledgments

The authors gratefully acknowledge the Office of Naval Research for funding under grant number N00014-21-1- 2069 with project monitor Steven Martens, Code 351 Jet Noise Reduction. The measurements were funded through the Advanced Pilot Training System Program Office and the Air Force Research Laboratory. The authors also thank Alan T. Wall for his contributions to the OLVR methodology and algorithms, as well as anonymous reviewers for their thoughtful and valuable feedback. Distribution A: Approved for public release; distribution unlimited. Cleared 05/12/2023.

References

[1] Wall, A. T., Gee, K. L., James, M. M., Bradley, K. A., McInerny, S. A., and Neilsen, T. B., "Near-Field Noise Measurements of a High-Performance Military Jet Aircraft," *Noise Control Engineering Journal*, Vol. 60, No. 4, 2012, pp. 421–434. https://doi.org/10.3397/1.3701021

[2] James, M. M., Salton, A. R., Downing, J. M., Gee, K. L., Neilsen, T. B., Reichman, B. O., McKinley, R. L., Wall, A. T., and Gallagher, H. L., "Acoustic Emissions from F-35 Aircraft During Ground Run-Up," *AIAA Aviation 2015 Forum*, AIAA Paper 2015-2375, June 2015. https://doi.org/10.2514/6.2015-2375

[3] Wall, A. T., Gee, K. L., Neilsen, T. B., McKinley, R. L., and James, M. M., "Military Jet Noise Source Imaging Using Multisource Statistically Optimized Near-Field Acoustical Holography," *Journal of the Acoustical Society of America*, Vol. 139, No. 4, 2016, pp. 1938–1950. https://doi.org/10.1121/1.4945719

[4] Tam, C. K. W., Aubert, A. C., Spyropoulos, J. T., and Powers, R. W., "On the Dominant Noise Components of Tactical Aircraft: Laboratory to Full Scale," *Journal of Sound and Vibration*, Vol. 422, May 2018, pp. 92–111. https://doi.org/10.1016/j.jsv.2018.02.023

[5] Leete, K. M., Wall, A. T., Gee, K. L., Neilsen, T. B., James, M. M., and Downing, J. M., "Acoustical Holography-Based Analysis of Spatiospectral Lobes in High-Performance Aircraft Jet Noise," *AIAA Journal*, Vol. 59, No. 10, 2021, pp. 4166–4178. https://doi.org/10.2514/1.J059400

[6] Leete, K. M., Vaughn, A. B., Bassett, M. S., Rasband, R. D., Novakovich, D. J., Gee, K. L., Campbell, S. C., Mobley, F. S., and Wall, A. T., "Jet Noise Measurements of an Installed GE F404 Engine," *AIAA SciTech Forum*, AIAA Paper 2021-1638, Jan. 2021. https://doi.org/10.2514/6.2021-1638

[7] Christian, M. A., Gee, K. L., Streeter, J. B., Mathews, L. T., Wall, A. T., Johnson, J. P., and Campbell, S. C., "Installed F404 Engine Noise Source Characteristics from Far-Field Directivity Measurements," *28th AIAA/CEAS Aeroacoustics Conference*, AIAA Paper 2022-3027, June 2022. https://doi.org/10.2514/6.2022-3027

[8] Olaveson, T., Ward, J. A., Johnson, J. P., Gee, K. L., and Wall, A. T., "Analysis of Spatiospectral Lobes in Installed F404 Engine Noise Radiation," *28th AIAA/CEAS Aeroacoustics Conference*, AIAA Paper 2022-3087, June 2022. https://doi.org/10.2514/6.2022-3087

[9] Murray, N. E., Tinney, C. E., and Panickar, P., "Laboratory-Scale Afterburning Supersonic Jet Noise Reduction Using Contoured Inserts," *28th AIAA/CEAS Aeroacoustics Conference*, AIAA Paper 2022-3030, June 2022. https://doi.org/10.2514/6.2022-3030

[10] Tam, C. K. W., and Parrish, S. A., "Noise of High-Performance Aircraft at Afterburner," *Journal of Sound and Vibration*, Vol. 352, Sept. 2015, pp. 103–128. https://doi.org/10.1016/j.jsv.2015.04.010

[11] Liu, J., Corrigan, A. T., Kailasanath, K., and Taylor, B. D., "Impact of the Specific Heat Ratio on the Noise Generation in a High-Temperature Supersonic Jet," *54th AIAA Aerospace Sciences Meeting*, AIAA Paper 2016-2125, Jan. 2016. https://doi.org/10.2514/6.2016-2125

[12] Arndt, R. E. A., Long, D. F., and Glauser, M. N., "The Proper Orthogonal Decomposition of Pressure Fluctuations Surrounding a Turbulent Jet," *Journal of Fluid Mechanics*, Vol. 340, June 1997, pp. 1–33. https://doi.org/10.1017/S0022112097005089

[13] Towne, A., Schmidt, O. T., and Colonius, T., "Spectral Proper Orthogonal Decomposition and Its Relationship to Dynamic Mode Decomposition and Resolvent Analysis," *Journal of Fluid Mechanics*, Vol. 847, July 2018, pp. 821–867. https://doi.org/10.1017/jfm.2018.283

[14] Schmidt, O. T., Towne, A., Rigas, G., Colonius, T., and Brès, G. A., "Spectral Analysis of Jet Turbulence," *Journal of Fluid Mechanics*, Vol. 855, Nov. 2018, pp. 953–982. https://doi.org/10.1017/jfm.2018.675

[15] Kwon, H. S., and Bolton, J. S., "Partial Field Decomposition in Nearfield Acoustical Holography by the Use of Singular Value Decomposition and Partial Coherence Procedures," *INTER-NOISE and NOISE-CON Congress and Conference Proceedings*, NOISE-CON 98, Ypsilanti MI, April 1998, pp. 649–654.

[16] Kim, Y. J., Bolton, J. S., and Kwon, H. S., "Partial Sound Field Decomposition in Multireference Near-Field Acoustical Holography by Using Optimally Located Virtual References," *Journal of the Acoustical Society of America*, Vol. 115, No. 4, 2004, pp. 1641–1652. https://doi.org/10.1121/1.1642627

[17] Wall, A. T., Gee, K. L., Leete, K. M., Nielsen, T. B., Stout, T. A., and James, M. M., "Partial-Field Decomposition Analysis of Full-Scale Supersonic Jet Noise Using Optimized-Location Virtual References," *Journal of the Acoustical Society of America*, Vol. 144, No. 3, 2018, pp. 1356–1367. https://doi.org/10.1121/1.5053580

[18] Long, D. F., "Jet Noise Source Location via Acoustic Holography and Shadowgraph Imagery," *14th AIAA/CEAS Aeroacoustics Conference (29th AIAA Aeroacoustics Conference)*, AIAA Paper 2008-2888, May 2008. https://doi.org/10.2514/6.2008-2888

[19] Vold, H., Shah, P. N., Davis, J., Bremmer, P. G., McLaughlin, D., Morris, P., Veltin, J., and McKinley, R., "High Resolution Continuous Scan Acoustical Holography Applied to High-Speed Jet Noise," *16th AIAA/CEAS Aeroacoustics Conference*, AIAA Paper 2010-3754, June 2010. https://doi.org/10.2514/6.2010-3754

[20] Neilsen, T. B., Gee, K. L., Wall, A. T., and James, M. M., "Similarity Spectra Analysis of High-Performance Jet Aircraft Noise," *Journal of the Acoustical Society of America*, Vol. 133, No. 4, 2013, pp. 2116–2125. https://doi.org/10.1121/1.4792360

[21] Neilsen, T. B., Vaughn, A. B., Gee, K. L., Swift, S. H., Wall, A. T., Downing, J. M., and James, M. M., "Three-Way Spectral Decompositions of High-Performance Military Aircraft Noise," *AIAA Journal*, Vol. 57, No. 8, 2019, pp. 3467–3479. https://doi.org/10.2514/1.J057992

[22] Tam, C. K. W., "Supersonic Jet Noise," *Annual Review of Fluid Mechanics*, Vol. 27, No. 1, 1995, pp. 17–43. https://doi.org/10.1146/annurev.fl.27.010195.000313

[23] Tam, C. K. W., Golebiowski, M., and Seiner, J. M., "On the Two Components of Turbulent Mixing Noise from Supersonic Jets," *2nd AIAA/CEAS Aeroacoustics Conference*, AIAA Paper 1996-1716, May 1996. https://doi.org/10.2514/6.1996-1716

[24] Tam, C. K. W., Viswanathan, K., Ahuja, K. K., and Panda, J., "The Sources of Jet Noise: Experimental Evidence," *Journal of Fluid Mechanics*, Vol. 615, Nov. 2008, pp. 253–292. https://doi.org/10.1017/S0022112008003704

[25] Tam, C. K. W., "Mach Wave Radiation from High-Speed Jets," *AIAA Journal*, Vol. 47, No. 10, 2009, pp. 2440–2448. https://doi.org/10.2514/1.42644
[26] Viswanathan, K., "Aeroacoustics of Hot Jets," *Journal of Fluid Mechanics*, Vol. 516, Oct. 2004, pp. 39–82. https://doi.org/10.1017/S0022112004000151
[27] Schlinker, R. H., Liljenberg, S. A., Polak, D. R., Post, K. A., Chipman, C. T., and Stern, A. M., "Supersonic Jet Noise Characteristics & Propagation: Engine and Model Scale," *13th AIAA/CEAS Aeroacoustics Conference (28th AIAA Aeroacoustics Conference)*, AIAA Paper 2007-3623, May 2007. https://doi.org/10.2514/6.2007-3623
[28] Epps, K. A., Merrill, C. D., Vaughn, A. B., Leete, K. M., Gee, K. L., and Wall, A. T., "Preliminary Similarity Spectra Analysis of Noise from a High-Performance Trainer Aircraft," *Proceedings of Meetings on Acoustics*, Vol. 42, No. 1, 2020, Paper 040006. https://doi.org/10.1121/2.0001623
[29] Prasad, C., and Morris, P. J., "Steady Active Control of Noise Radiation from Highly Heated Supersonic Jets," *Journal of the Acoustical Society of America*, Vol. 149, No. 2, 2021, pp. 1306–1317. https://doi.org/10.1121/10.0003570
[30] Jordan, P., and Colonius, T., "Wave Packets and Turbulent Jet Noise," *Annual Review of Fluid Mechanics*, Vol. 45, Jan. 2013, pp. 173–195. https://doi.org/10.1146/annurev-fluid-011212-140756
[31] Liu, J., and Ramamurti, R., "Numerical Study of Supersonic Jet Noise Emanating from an F404 Nozzle at Model Scale," *AIAA SciTech 2019 Forum*, AIAA Paper 2019-0807, Jan. 2019. https://doi.org/10.2514/6.2019-0807
[32] Ennix, K. A., Burcham, F. W., and Webb, L. D., "Flight-Determined Engine Exhaust Characteristics of an F404 Engine in an F-18 Airplane," *29th Joint Propulsion Conference and Exhibit*, AIAA Paper 1993-2543. See also NASA TM-4538, June 1993. https://doi.org/10.2514/6.1993-2543
[33] Seiner, J. M., Ukeiley, L. S., and Jansen, B. J., "Aero-Performance Efficient Noise Reduction for the F404-400 Engine," *11th AIAA/CEAS Aeroacoustics Conference*, AIAA Paper 2005-3048, May 2005. https://doi.org/10.2514/6.2005-3048
[34] Christian, M. A., and Gee, K. L., "Connecting the Convective Mach Number to Full-Scale Supersonic Jet Noise Directivity," *AIAA Aviation 2023 Forum*, AIAA Paper 2023-3351, June 2023. https://doi.org/10.2514/6.2023-3351
[35] Goates, C. B., Harker, B. M., Neilsen, T. B., and Gee, K. L., "Extending the Bandwidth of an Acoustic Beamforming Array Using Phase Unwrapping and Array Interpolation," *Journal of the Acoustical Society of America*, Vol. 141, No. 4, 2017, Paper EL407. https://doi.org/10.1121/1.4981235
[36] Harker, B. M., Gee, K. L., Neilsen, T. B., Wall, A. T., and James, M. M., "Source Characterization of Full-Scale Tactical Jet Noise from Phased-Array Measurements," *Journal of the Acoustical Society of America*, Vol. 146, No. 1, 2019, pp. 665–680. https://doi.org/10.1121/1.5118239
[37] Cook, M. R., Gee, K. L., Sommerfeldt, S. D., and Neilsen, T. B., "Coherence-Based Phase Unwrapping for Broadband Acoustic Signals," *Proceedings of Meetings on Acoustics*, Vol. 30, No. 2, 2017, Paper 055005. https://doi.org/10.1121/2.0000611
[38] Shah, P. N., Vold, H., and Yang, M., "Reconstruction of Far-Field Noise Using Multireference Acoustical Holography Measurements of High-Speed Jets," *17th AIAA/CEAS Aeroacoustics Conference (32nd AIAA Aeroacoustics Conference)*, AIAA Paper 2011-2772, June 2011. https://doi.org/10.2514/6.2011-2772
[39] Lee, M., and Bolton, J. S., "Source Characterization of a Subsonic Jet by Using Near-Field Acoustical Holography," *Journal of the Acoustical Society of America*, Vol. 121, No. 2, 2007, pp. 967–977. https://doi.org/10.1121/1.2404626
[40] Long, D., Peters, J., and Anderson, M., "Evaluating Turbofan Exhaust Noise and Source Characteristics from Near Field Measurements," *15th AIAA/CEAS Aeroacoustics Conference (30th AIAA Aeroacoustics Conference)*, AIAA Paper 2009-3214, May 2009. https://doi.org/10.2514/6.2009-3214
[41] Wall, A. T., Gee, K. L., and Neilsen, T. B., "Multisource Statistically Optimized Near-Field Acoustical Holography," *Journal of the Acoustical Society of America*, Vol. 137, No. 2, 2015, pp. 963–975. https://doi.org/10.1121/1.4906585
[42] Hald, J., "Basic Theory and Properties of Statistically Optimized Near-Field Acoustical Holography," *Journal of the Acoustical Society of America*, Vol. 125, No. 4, 2009, pp. 2105–2120. https://doi.org/10.1121/1.3079773
[43] Williams, E. G., "Continuation of Acoustic Near-Fields," *Journal of the Acoustical Society of America*, Vol. 113, No. 13, 2003, pp. 1273–1281. https://doi.org/10.1121/1.1528173
[44] Leete, K. M., Wall, A. T., Gee, K. L., Neilsen, T. B., Harker, B. M., and James, M. M., "Azimuthal Coherence of the Sound Field in the Vicinity of a High Performance Military Aircraft," *Proceedings of Meetings on Acoustics*, Vol. 29, No. 1, 2016, Paper 045007. https://doi.org/10.1121/2.0000673
[45] Steiner, R., and Hald, J., "Near-Field Acoustical Holography Without the Errors and Limitations Caused by the Use of Spatial DFT," *International Journal of Acoustics and Vibration*, Vol. 6, No. 2, 2001, pp. 83–89. https://doi.org/10.20855/ijav.2001.6.278
[46] Williams, E. G., "Regularization Methods for Near-Field Acoustical Holography," *Journal of the Acoustical Society of America*, Vol. 110, No. 4, 2001, pp. 1976–1988. https://doi.org/10.1121/1.1404381
[47] Stout, T. A., Wall, A. T., Gee, K. L., and Neilsen, T. B., "Obtaining Acoustic Intensity from Multisource Statistically Optimized Near-Field Acoustical Holography," *Proceedings of Meetings on Acoustics*, Vol. 33, No. 1, 2018, Paper 055002. https://doi.org/10.1121/2.0000835
[48] Schmidt, R. O., "A Signal Subspace Approach to Multiple Emitter Location and Spectral Estimation," Ph.D. Dissertation, Stanford Univ., Stanford, CA, Nov. 1981.
[49] Schmidt, R. O., "Multiple Emitter Location and Signal Parameter Estimation," *RADC Spectrum Estimation Workshop*, Oct. 1979, Griffiss Air Force Base, NY. Reproduced as: Schmidt, R. O., "Multiple Emitter Location and Signal Parameter Estimation," *IEEE Transactions on Antennas and Propagation*, Vol. 34, No. 3, 1986, pp. 276–280. https://doi.org/10.1109/TAP.1986.1143830
[50] Johnson, D. H., and Dudgeon, D. E., *Array Signal Processing: Concepts and Techniques*, Prentice-Hall, Englewood Cliffs, NJ, 1993, pp. 382–385.
[51] Bendat, J. S., "Modern Analysis Procedures for Multiple Input/Output Problems," *Journal of the Acoustical Society of America*, Vol. 68, No. S1, 1980, pp. 498–503. https://doi.org/10.1121/1.384760
[52] Eldred, K. M., "Acoustic Loads Generated by the Propulsion System," NASA SP-8072, 1971.
[53] Lubert, C. P., Gee, K. L., and Tsutsumi, S., "Supersonic Jet Noise from Launch Vehicles: 50 Years Since NASA SP-8072," *Journal of the Acoustical Society of America*, Vol. 151, No. 2, 2022, pp. 752–791. https://doi.org/10.1121/10.0009160
[54] Olaveson, T. W., Gee, K. L., and Johnson, J. P., "Wavelet-Based Analysis of Spectral and Temporal Structures in F404 Engine Jet Noise," *AIAA Aviation 2023 Forum*, AIAA Paper 2023-3213, June 2023. https://doi.org/10.2514/6.2023-3213
[55] Swift, S. H., Gee, K. L., Neilsen, T. B., Wall, A. T., Downing, J. M., and James, M. M., "Spatiotemporal Correlation Analysis of Jet Noise from a Round-Nozzle Supersonic Aircraft," *2018 AIAA/CEAS Aeroacoustics Conference*, AIAA Paper 2018-3938, June 2018. https://doi.org/10.2514/6.2018-3938
[56] Mathews, L. T., Gee, K. L., Leete, K. M., and Wall, A. T., "Acoustic Source Characterization of an Installed GE F404 Engine Using Near-Field Acoustical Holography," *28th AIAA/CEAS Aeroacoustics Conference*, AIAA Paper 2022-3028, June 2022. https://doi.org/10.2514/6.2022-3028
[57] Mathews, L. T., Gee, K. L., and Wall, A. T., "Coherence-Based Acoustic Source Decomposition of Installed GE F404 Engine Noise," *AIAA Aviation 2023 Forum*, AIAA Paper 2023-3212, June 2023. https://doi.org/10.2514/6.2023-3212
[58] Leete, K. M., Gee, K. L., Liu, J., and Wall, A. T., "Coherence Analysis of the Noise from a Simulated Highly Heated Laboratory-Scale Jet," *AIAA Journal*, Vol. 58, No. 8, 2020, pp. 3426–3435. https://doi.org/10.2514/1.J059112
[59] Liu, J., Corrigan, A. T., Kailasanath, K., and Gutmark, E. J., "Impact of Chevrons on Noise Source Characteristics in Imperfectly Expanded Jet Flows," *21st AIAA/CEAS Aeroacoustics Conference*, AIAA Paper 2015-2835, June 2015. https://doi.org/10.2514/6.2015-2835
[60] Liu, J., Kailasanath, K., and Gutmark, E. J., "Similarity Spectra Analysis in Highly Heated Supersonic Jets Using Large-Eddy Simulations," *55th AIAA Aerospace Sciences Meeting*, AIAA Paper 2017-0926, Jan. 2017. https://doi.org/10.2514/6.2017-0926
[61] Nagamatsu, H. T., Sheer, R. E., and Horvay, G., "Supersonic Jet Noise Theory and Experiments," Basic Aerodynamic Noise Research, NASA SP-207, 1969.

[62] Nagamatsu, H. T., and Horvay, G., "Supersonic Jet Noise," *8th Aerospace Sciences Meeting*, AIAA Paper 1970-0237, Jan. 1970. https://doi.org/10.2514/6.1970-237

[63] Gee, K. L., "A Tale of Two Curves and Their Influence on Rocket and Supersonic Jet Noise Research," *Journal of the Acoustical Society of America*, Vol. 149, No. 4, 2021, pp. 2159–2162. https://doi.org/10.1121/10.0003938

[64] Baars, W. J., Murray, N. E., and Tinney, C. E., "A Proper Framework for Studying Noise from Jets with Non-Compact Sources," *Journal of Fluid Mechanics*, Vol. 929, Dec. 2021, Paper A23. https://doi.org/10.1017/jfm.2021.837

[65] Harker, B. M., Gee, K. L., Neilsen, T. B., Wall, A. T., and James, M. M., "Beamforming-Based Wavepacket Model for Noise Environment Predictions of Tactical Aircraft," *23rd AIAA/CEAS Aeroacoustics Conference*, AIAA Paper 2017-4048, June 2017. https://doi.org/10.2514/6.2017-4048

[66] Wall, A. T., Gardner, M. D., Gee, K. L, and Neilsen, T. B., "Coherence Length as a Figure of Merit in Multireference Near-Field Acoustical Holography," *JASA Express Letters*, Vol. 132, No. 3, 2012, Paper EL215. https://doi.org/10.1121/1.4740518

[67] Olaveson, T., Harker, B. M., and Gee, K. L., "Beamforming-Based Wavepacket Model for Noise Predictions of Tactical Aircraft," *Proceedings of Meetings on Acoustics*, Vol. 29, No. 1, 2016, Paper 040011. https://doi.org/10.1121/2.0001639

[68] Papamoschou, D., "Wavepacket Modeling of the Jet Noise Source," *17th AIAA/CEAS Aeroacoustics Conference (32nd AIAA Aeroacoustics Conference)*, AIAA Paper 2011-2835, June 2011. https://doi.org/10.2514/6.2011-2835

[69] Harker, B. M., Neilsen, T. B., Gee, K. L., Wall, A. T., and James, M. M., "Spatiotemporal Correlation Analysis of Jet Noise from a High-Performance Military Aircraft," *AIAA Journal*, Vol. 54, No. 5, 2016, pp. 1554–1566. https://doi.org/10.2514/1.J054442

[70] Wall, A. T., Gee, K. L., Neilsen, T. B., Harker, B. M., McInerny, S. A., McKinley, R. L., and James, M. M., "Investigation of Multi-Lobed Fighter Jet Noise Sources Using Acoustical Holography and Partial Field Decomposition Methods," *21st AIAA/CEAS Aeroacoustics Conference*, AIAA Paper 2015-2379, June 2015. https://doi.org/10.2514/6.2015-2379

[71] Panda, J., Seasholtz, R. G., and Elam, K. A., "Investigation of Noise Sources in High-Speed Jets via Correlation Measurements," *Journal of Fluid Mechanics*, Vol. 537, Aug. 2005, pp. 349–385. https://doi.org/10.1017/S0022112005005148

[72] Viswanathan, K., "Investigation of the Sources of Jet Noise," *13th AIAA/CEAS Aeroacoustics Conference (28th AIAA Aeroacoustics Conference)*, AIAA Paper 2007-3601, May 2007. https://doi.org/10.2514/6.2007-3601

[73] Unnikrishnan, S., and Gaitonde, D. V., "A Pressure Decomposition Framework for Aeroacoustic Analysis of Turbulent Jets," *European Journal of Mechanics/B Fluids*, Vol. 81, May 2018, pp. 41–61. https://doi.org/10.1016/j.euromechflu.2020.01.006

C. Bailly
Associate Editor